Raman Lidar Measurements during the International H_2O Project. Part I: Instrumentation and Analysis Techniques

D. N. WHITEMAN,* B. DEMOZ,* P. DI GIROLAMO,+ J. COMER,# I. VESELOVSKII,@ K. EVANS,@ Z. WANG,& M. CADIROLA,** K. RUSH,* G. SCHWEMMER,* B. GENTRY,* S. H. MELFI,@ B. MIELKE,++ D. VENABLE,## AND T. VAN HOVE@@

*NASA GSFC, Greenbelt, Maryland
+DIFA, University of Basilicata, Potenza, Italy
#Science Systems Applications, Inc., Lanham, Maryland
@University of Maryland, Baltimore County, Baltimore, Maryland
&University of Wyoming, Laramie, Wyoming
**Ecotronics LLC, Clarksburg, Maryland
++Licel Corporation, Berlin, Germany
##Howard University, Washington, D.C.
@@University Corporation for Atmospheric Research, Boulder, Colorado

(Manuscript received 23 March 2005, in final form 14 July 2005)

ABSTRACT

The NASA Goddard Space Flight Center (GSFC) Scanning Raman Lidar (SRL) participated in the International H_2O Project (IHOP), which occurred in May and June 2002 in the midwestern part of the United States. The SRL received extensive optical modifications prior to and during the IHOP campaign that added new measurement capabilities and enabled unprecedented daytime water vapor measurements by a Raman lidar system. Improvements were also realized in nighttime upper-tropospheric water vapor measurements. The other new measurements that were added to the SRL for the IHOP deployment included rotational Raman temperature, depolarization, cloud liquid water, and cirrus cloud ice water content. In this first of two parts, the details of the operational configuration of the SRL during IHOP are provided along with a description of the analysis and calibration procedures for water vapor mixing ratio, aerosol depolarization, and cirrus cloud extinction-to-backscatter ratio. For the first time, a Raman water vapor lidar calibration is performed, taking full account of the temperature sensitivity of water vapor and nitrogen Raman scattering. Part II presents case studies that permit the daytime and nighttime error statistics to be quantified.

1. Introduction

The International H_2O Project (IHOP) was the largest meteorological field campaign ever held in the United States (Weckwerth et al. 2004). It occurred in the Midwestern United States between 13 May and 25 June 2002. The goal of IHOP was to measure convective storm systems with sufficient detail to permit quantitative precipitation and convection initiation forecasting to be improved. During IHOP, numerous intensive operation periods were declared, focusing on boundary layer evolution, drylines, bores, nocturnal jets, and other mesoscale events. IHOP included participants from numerous U.S. and foreign government agencies as well as universities.

The instrumentation used during IHOP included seven research aircraft carrying three water vapor lidars and one wind lidar, mobile radar systems for storm chasing, and a ground-based site in the western panhandle of Oklahoma that included the National Aeronautics and Space Administration (NASA) Goddard Space Flight Center (GSFC) Scanning Raman Lidar (SRL), Goddard Lidar Observatory for Winds (GLOW) molecular wind lidar (Gentry et al. 2004), and the Holographic Airborne Rotating Lidar Instrument Experiment (HARLIE) (Schwemmer et al. 2004) scanning aerosol lidar. Other instruments that were located at the western Oklahoma site that came to be known as

Corresponding author address: D. N. Whiteman, NASA GSFC, Code 613.1, Building 33, Room D404, Greenbelt, MD 20771.
E-mail: david.n.whiteman@nasa.gov

"Homestead" were Vaisala RS-80 G15H and Snow-White radiosonde systems (Wang et al. 2003), cloud and aerosol radar, sodar, Atmospheric Emitted Radiance Interferometer (AERI) (Feltz et al. 1998), Suomi-Net global positioning system (GPS) (Ware et al. 2000), and an Aerosol Robotic Network (AERONET) (Holben et al. 1998) sun photometer.

This first of two papers provides a detailed description of the experimental configuration of the NASA GSFC SRL during its participation in IHOP. This configuration provided measurements of water vapor mixing ratio, aerosol backscatter, extinction and depolarization, rotational Raman temperature measurements performed in the UV (Di Girolamo et al. 2004), cloud liquid water (Russo et al. 2004), and cirrus cloud particle size and ice water content (Wang et al. 2004). All of these measurements were made using a single output wavelength of 354.7 nm, demonstrating the feasibility of providing these measurements in an automated and eye-safe system (Di Girolamo et al. 2004). Particular attention will be given here to the instrumentation and analysis techniques that led to improved daytime water vapor measurement capability. With these improvements, it is now possible to use a single experimental configuration for quantifying water vapor variation in the boundary layer during the daytime and extending into the upper troposphere at night. The paper is structured as follows. The instrumental configuration of the SRL for the IHOP campaign is first detailed. The techniques for processing the raw data and of calculating water vapor mixing ratio, aerosol scattering ratio, aerosol depolarization, and cirrus cloud extinction to backscatter ratio are then presented. In the second part of this paper (Whiteman et al. 2006, hereafter referred to as Part II) comparisons of the SRL water vapor measurements with those of other instruments at IHOP are presented along with daytime and nighttime case studies that demonstrate measurement capability and permit the error characteristics to be quantified.

2. The pursuit of non-solar-blind daytime Raman water vapor lidar measurements

During IHOP, the SRL demonstrated greatly improved non-solar-blind daytime Raman water vapor lidar measurements over any previously demonstrated. The combination of technologies and techniques that permitted this were 1) a large-pulse tripled Nd:YAG laser, 2) narrow-field-of-view (FOV) telescope, 3) narrow spectral band detection, 4) fast photomultiplier detectors, and 5) a combination of analog and photon-counting electronics, which permit the full intensity Raman signals to be sampled. While none of these elements is new, the combination had not been fully exploited previously for Raman water vapor lidar. Furthermore, the path toward this solution was not direct and occurred over more than 20 yr of research activity at various research centers. The history of this development can be found online at http://ramanlidar.gsfc.nasa.gov or by contacting the authors.

3. The Scanning Raman Lidar

Development of the NASA GSFC Scanning Raman Lidar began in 1989 under the support of both NASA and the Department of Energy's (DOE) Instrument Development Program (IDP). The SRL was first deployed in the field in November 1991 for the Spectral Radiance Experiment (Ellingson and Wiscombe 1996), which was sponsored by NASA and DOE and took place in Coffeyville, Kansas. At that time the system was based on a Lambda Physik LPX 240iCC excimer laser that produced up to 30 W at 351 nm using a XeF gas mixture and up to 100 W at 248 nm using a KrF gas mixture. Nighttime measurements were performed using the 351-nm output of the laser, and daytime measurements (Whiteman et al. 1994) were made using the 248-nm output and the solar-blind technique (Renaut and Capitini 1988; Renaut et al. 1980; Cooney et al. 1985) whereby solar background is essentially eliminated by absorption due to stratospheric ozone. The use of the solar-blind technique requires a knowledge of the tropospheric ozone profile so that the differential extinction of the H_2O and N_2 signals by ozone can be accounted for in the water mixing ratio calculation. This approach to Raman water vapor measurements permitted photon-counting data acquisition (100 MHz in the initial implementation of the SRL) to be used exclusively. The solar-blind measurements of water vapor using the SRL were hampered by the large attenuation of the outgoing laser radiation due to tropospheric ozone, which caused signal-induced-noise (SIN) problems in the photomultiplier tube (PMT) detectors in use at the time. The PMTs were upgraded in 1993 to ones with significantly lower SIN problems, but still overlap problems prevented an accurate quantification of the ozone profile in the lowest 1 km (Whiteman et al. 1994). Also, the absorption cross section of ozone does not differ greatly between the Raman-shifted returns for N_2 and O_2 when excited by 248 nm (Goldsmith and Ferrare 1994; Whiteman et al. 1994). This degrades the sensitivity of the technique for deriving ozone. Theoretical modeling (Goldsmith and Ferrare 1994) indicates that a longer excitation wavelength of approximately 260 nm would be greatly preferred for solar-blind measurements. Nonetheless, daytime solar-blind water vapor mixing ratio measurements were made

with the SRL in 1993 to an altitude of 2.5 km using a 20-min average (Whiteman et al. 1994).

The narrow spectral band, narrow-field-of-view technique for making Raman water vapor lidar measurements was also explored with the SRL in 1992 using the XeF (351 nm) output of the excimer laser. These measurements were performed by expanding the laser beam by a factor of 5 and using a 0.5-mrad field of view. However, the 100-MHz photon-counting data acquisition system, fully sufficient for the original solar-blind conception of the SRL, was incapable of handling the high count rates present in non-solar-blind daytime Raman lidar measurements. Thus, the input signals required attenuation by more than two orders of magnitude to permit them to be photon counted. Nonetheless, daytime measurements were performed through the boundary layer with 1-h averaging (Whiteman et al. 1994). In the early 1990s, therefore, we had determined that addition of analog electronics would be necessary to optimize daytime measurements using the narrowband, narrow-field-of-view technique.

It was also clear that, considering a fixed amount of output power, a smaller number of larger laser pulses offered significant advantages for daytime operations (Bisson et al. 1999) over a larger number of smaller pulses. Therefore, in 1995, a Nd:YAG laser was added to the SRL in preparation for the Tropospheric Aerosol Radiation Field Observational Experiment (TARFOX) field campaign (Ferrare et al. 2000). Narrow spectral band, narrow-field-of-view measurements of water vapor were performed using the SRL during TARFOX and can be seen at our Web site (http://ramanlidar.gsfc.nasa.gov); however, the 100-MHz photon-counting data system was still in use, requiring that the input signals be attenuated by at least an order of magnitude in order to limit the photon arrival rate. In addition, the interference filters available at the time were limited to approximately 25% transmission for a 0.5-nm passband.

Additional technology development and the SRL configuration for IHOP

Drawing on the previous experience gained in Raman water vapor lidar development, in 1998 we began construction of the Raman Airborne Spectroscopic Lidar (RASL) under the NASA Instrument Incubator Program (IIP). The goal of this instrument was to bring the range of Raman lidar water vapor and aerosol measurements to an airborne platform and to take advantage of performance enhancements that are realized by measuring downward in the atmosphere versus measuring upward (Whiteman et al. 2001b). This new development effort included the purchase of a new data acquisition system from Licel of Berlin, Germany, that incorporates both analog and photon-counting electronics and that circumvented one of the limitations of the earlier daytime Raman water vapor lidar measurements. The RASL data acquisition system was used in the SRL for the IHOP field deployment. By the time of IHOP, significantly improved interference filters were also available for Raman water vapor measurements. These two enhancements were critical to the successful water vapor measurements made by the SRL during IHOP.

Many additional modifications were made to the SRL immediately prior to and during the IHOP field campaign. Substantially new wavelength separation optics were implemented on the large 0.76-m F/5.2 Dall-Kirkham telescope. This provided simultaneous measurements of water vapor mixing ratio, aerosol backscatter and extinction, cloud liquid (Whiteman and Melfi 1999; Russo et al. 2004) and ice water (Wang et al. 2004), and rotational Raman temperature (Di Girolamo et al. 2004). In addition, a 0.25-m F/2.5 Newtonian telescope was added in the field during the IHOP experiment for the low-altitude Raman measurements, accomplished via fiber optic coupling, and for aerosol depolarization measurements using free-space coupled optics. The fiber-coupled measurements from this telescope were not useful during IHOP due to an improperly coated mirror. Because of this problem, most data products were processed to a minimum altitude of 300 m, the lowest altitude to which the data from the large telescope were useful. The laser used was the same laser that was installed in the SRL prior to the TARFOX field campaign: a continuum-tripled Nd:YAG laser operating at 354.7 nm operating at 30 Hz and generating approximately 9 W of output power. The fields of view of the large and small telescopes were approximately 0.3 and 1.2 mrad, respectively. The narrow field-of-view of the large telescope coupled with narrow spectral filters in the water vapor and nitrogen channels (0.25 and 0.28 nm, respectively) and the combined use of analog and photon-counting data acquisition permitted the full intensity water vapor and nitrogen signals to be sensed throughout the diurnal cycle with no instrumental changes occurring during the measurements. The previous configuration of the SRL required attenuation filters during the daytime due to the high solar background. The addition of analog data acquisition electronics and narrow spectral bandpass filters now permits the full intensity signal to be sampled diurnally. This enabled the water vapor mixing ratio to be quantified during the daytime at significantly higher temporal and spatial resolution than was previously possible. Table 1 shows the specifications of the SRL

TABLE 1. Hardware and optical configuration of the NASA GSFC Scanning Raman Lidar during the IHOP field campaign.

NASA GSFC Scanning Raman Lidar specifications for the IHOP field campaign		
Component	Description	Notes
Laser	Continuum custom long cavity Nd:YAG tripled; 30 Hz, 300 mj pulse^{-1}	Converted to closely emulate model 9030
Telescope (high altitude)	Starr Optical, Dall-Kirkham, 0.76 m, F/5.2 horizontally mounted	Variable FOV, but nomimally 0.3 mrad
Telescope (low altitude)	Custom Newtonian, 0.25 m, F2.5	1.2 mrad field of view; new for IHOP
Spectrum analyzer	Custom designed using Barr dichroic beamsplitters and interference filters	
Measurement/filter—Large telescope		
Rotational Raman [352(1.2 nm)$^{-1}$]		New for IHOP
Rotational Raman [354(0.3 nm)$^{-1}$]		New for IHOP
Rayliegh–Mie [354.7(0.3 nm)$^{-1}$]		
Raman nitrogen [386.7(0.3 nm)$^{-1}$]		
Raman liquid/ice water [403(6.0 nm)$^{-1}$]		New for IHOP
Raman water vapor [407.6(0.25 nm)$^{-1}$]	Now tilt tuned to center at 407.45 nm	
Measurement/filter—Small telescope		
Rayleigh–Mie [354.7/0.3 nm)$^{-1}$]	Fiber coupled	New for IHOP
Perpendicular polarization [354.7(0.3 nm)$^{-1}$]	Direct coupled	New for IHOP
Parallel polarization [354.7(0.3 nm)$^{-1}$]	Direct coupled	New for IHOP
Raman nitrogen [386.7(0.3 nm)$^{-1}$]	Fiber coupled	New for IHOP
Raman liquid/ice water [403(6.0 nm)$^{-1}$]	Fiber coupled	New for IHOP
Raman water vapor [407.65(0.25 nm)$^{-1}$]	Now tilt tuned to center at 407.45 nm	New for IHOP
Scanning mirror	Starr Optical, 1.1 m × 0.8 m flat, 50-mm thickness	
Scan motor assembly	Custom twin-axle, belt-drive design with 22-bit shaft encoder	
PMTs	Hamamatsu R1924 (selected for high gain, high blue sensitivity and low dark counts) and R7400	
PMT housings	Products for research	
Data acquisition system	Licel analog + photon-counting transient recorders (7.5-m spatial resolution)	
Data acquisition computer	Personal computer running Windows 2000	

during IHOP and notes the components/measurements that were new for IHOP.

4. Data analysis techniques

Numerous atmospheric quantities were measured by the SRL during IHOP as shown in Table 1. The analytical procedures for the particular measurements of concern in this paper are described in this section. For all of these measurements, however, the first step in the analysis is combining the analog-to-digital (AD) and photon-counting (PC) data into a single composite profile for each signal measured. That procedure will now be described.

a. Combined analog and photon-counting data—"Gluing"

The Licel data acquisition electronics in use in the SRL measure a lidar signal simultaneously using 20-MHz, 12-bit analog to digital converters and 250-MHz photon counters. Two separate data streams are maintained within the instruments that must be merged in some fashion to create a final output profile for each channel. The process of combining the analog and photon-counting data together has come to be known as "gluing." After experimenting with various methods of calculating the conversion between an analog voltage and a photon count rate, the following procedure was used to determine mean conversion factors that are used to convert the analog data to a "virtual" count rate scale.

The photon-counting data are first corrected for photon pulse pile-up assuming the photon-counting circuitry behaves in a nonparalyzable fashion (Whiteman et al. 1992; Whiteman 2003a). The background is subtracted separately from the analog and photon-counting records. Then, ordered pairs of AD and PC

data are formed in a region of the signal where both are considered to be responding linearly, and that avoids problem areas such as near the time when the laser fires. The low and high count rate thresholds that define this region are typically 1 and 10–20 MHz, respectively, for our Hamamatsu 1924 PMTs, which possess a pulse width of 4–5 ns. The points in the AD and PC profiles that fall within these ranges and satisfy the other conditions are then formed as ordered pairs, and a linear regression is performed on these points. As an additional noise filter, the residuals between the actual data points and the best-fit linear regression are then calculated and any points outside of two standard deviations from the mean are excluded. For the Rayleigh–Mie channels, additional noise filtering using 95% quantile regression was sometimes required. This regression technique is illustrated in the upper and middle plots of Fig. 1. In the upper plot, the regression of the AD and PC ordered pairs is shown with and without the application of the photon pulse pile-up correction. The slope [MHz $(\text{mV})^{-1}$] and offset (in MHz) of the regressions are given in the figure. Notice that the regression of the pulse pile-up corrected data exhibits a slope approximately 10% higher than the uncorrected data. Also, the offset of the corrected data is much closer to zero. The middle plot of the figure is a blowup of the portion of the regression near the origin to permit the offsets to be seen more clearly. Since the background has already been subtracted separately from the analog and photon-counting data, the value of the optimum resolving time can be determined by studying the offset versus the resolving time used in the pile-up correction. The optimum resolving time is the one that yields an offset closest to zero. This technique can be contrasted with what was done previously to determine the optimum resolving time using purely PC systems (Whiteman et al. 1992; Whiteman 2003a) where a significantly attenuated version of the signal was used as the linear signal instead of the analog signal as used here. The technique illustrated here should be valid as long as the nonparalyzable equation properly describes the counting behavior of the electronics and the analog electronics are providing linear measurements. The nonparalyzable equation is certainly just an approximation of the counting behavior of the electronics so it is important to limit the maximum count rate of the data used to determine the optimum value of the resolving time. The analysis of the offset versus resolving time shown in the lower panel of Fig. 1, performed using a count rate range of 1–20 MHz, shows that ~5 ns is the optimum value. For comparison, the rms differences between the nonparalyzable model and the actual data points are also shown as a function of resolving time. There is a poorly defined minimum at approximately 2 ns. We do not consider this determination of the resolving time to be reliable due to the very shallow minimum in the rms curve. The minimum becomes better defined using this technique if higher count rates are permitted in the regression. However, considering that the nonparalyzable correction already amounts to ~11% at 20 MHz using 5 ns for the resolving time, determining the optimum resolving time using higher count rates will be more subject to errors introduced by the assumption that the electronics behave in a purely nonparalyzable fashion. Therefore, we choose to determine the optimum resolving time based on the zero crossing for the offset.

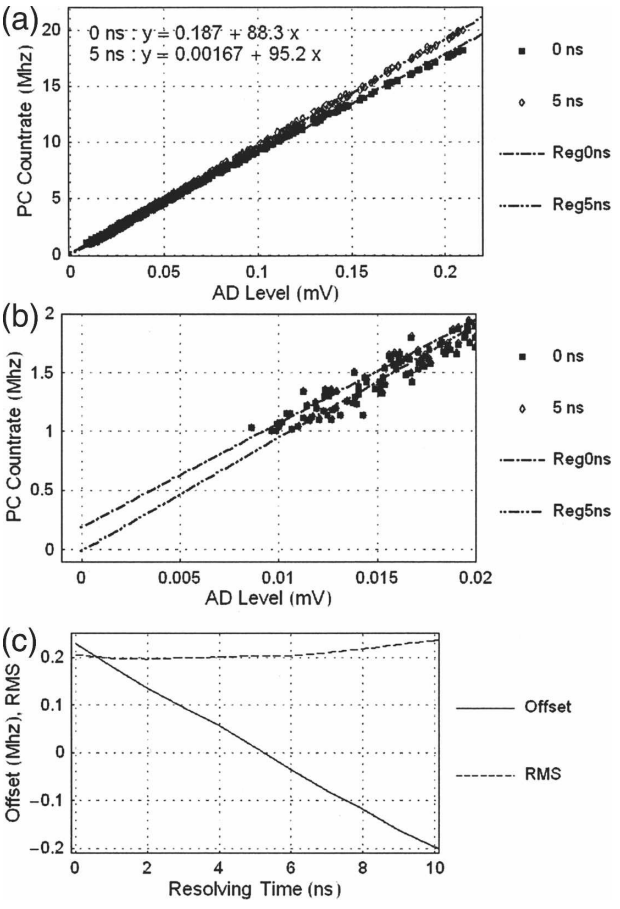

FIG. 1. (a) Two regressions of AD–PC data pairs are shown, before and after the correction for pulse pile up. (b) The same data as (a) but a blowup near the origin to show the intercept values more clearly. (c) Calculated offset of the linear regression vs resolving time value. The optimum resolving time of ~5 ns produces a near-zero offset. For comparison, the rms of the residuals for each regression is also shown. This method of determining the optimum resolving time is less sensitive than the offset approach.

GLUING COEFFICIENTS AND WATER VAPOR MIXING RATIO CALIBRATION

Variations in the Raman lidar water vapor mixing ratio calibration can have important consequences for meteorological application of Raman lidar measurements. Therefore, it is important to study the behavior of the AD to PC conversion factors under differing conditions. In particular, the behavior of the slopes of the regressions as the background is increasing due to increased solar radiation is of particular interest. Data acquired on 19–20 June 2002, when several wave events could be observed in the water vapor field, will now be used to illustrate the gluing process.

The times series of fully calibrated water vapor mixing ratio is presented in Fig. 2a. As will be discussed in section 4b, the water vapor mixing ratio calculation is performed using the Raman water vapor and nitrogen measurements. Figures 2b and 2c therefore show which portions of the fully processed water vapor image shown in Fig. 2a used AD (shown in white) and PC (black) data from the water vapor (Fig. 2b) and nitrogen (Fig. 2c) signals. One can see that for daytime measurements only analog data were used whereas during the nighttime a combination of AD and PC are used. It is during the periods of reduced solar background when the gluing process can be used in the Raman channels. A time series of the gluing conversion factors is therefore presented in Fig. 2d for both the water vapor signal and the nitrogen signals where a transition period between daytime and nighttime measurements has been chosen. At the beginning of the period shown, mean photon-counting signals exceed 20 MHz and therefore a regression between AD and PC data was not performed. At approximately 0150 UTC (indicated as 2550 in the figure), the solar background decreased to the point where it was possible to perform the regression. But as the figure shows, the regressions that occur during the transition from day to night are characterized by low correlation coefficients ($R^2 \times 10$) and significantly changing slopes. Through experimentation, it was determined that good quality regressions resulted if the mean background count rate was below the minimum threshold frequency set to be 1 MHz in this example. The time at which this transition occurred (~2610 UTC) is indicated by the vertical line (Trans) in the figure. The calculated slopes and correlation coefficients (R^2) tend to decrease quickly to the left of this line, which defines the region where the background points qualify for the regression. To the right of this line the mean H_2O [indicated by $m(H_2O)$] and N_2 [$m(N_2)$] slopes are $\sim 8.4 \pm 0.08 \times 10^{10}$ and $9.5 \pm 0.03 \times 10^{10}$ HzV^{-1} [10^{10} HzV^{-1} = 10 $MHz(mV)^{-1}$], respectively.

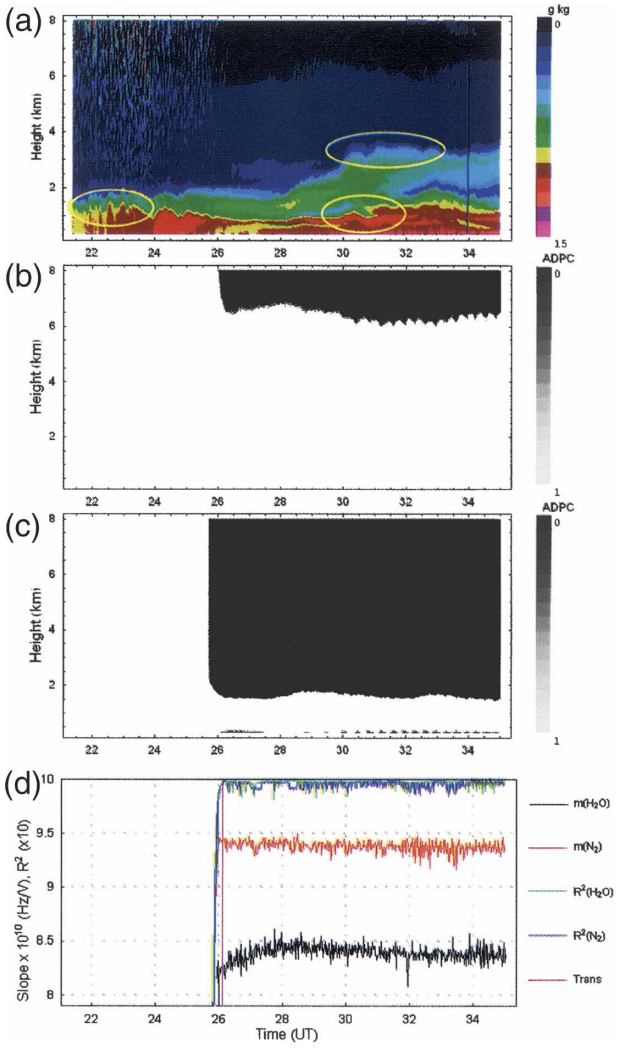

FIG. 2. (a) Water vapor mixing ratio variation during the period of 19–20 Jun 2002 in IHOP. Three wave regions are encircled. The major bore event was at ~30.5 UTC and 0.5 km. (b) Diagram indicating the use of either AD (white) or PC data (black) for the nitrogen data used in calculating the water vapor mixing shown in (a). (c) Diagram indicating the use of either AD (white) or PC data (black) for the water vapor data used in calculating the water vapor mixing shown in (a). (d) Time series of slopes of the regressions used to determine the coefficients to convert analog data to a virtual photon-counting scale.

The N_2 slope is quite constant beyond the transition point but, even though the variation in the H_2O slope beyond the transition point is less than 1%, the slight tendency for the H_2O slope to increase with time is still under investigation.

Even though good quality regressions are obtained under most circumstances using the technique just described, the profile-to-profile conversion factor between AD and PC is subject to statistical fluctuations that likely do not reflect variation in the gain of the

electronics. Therefore, it is desirable to use a single conversion factor for each channel for an entire data record. For the IHOP data processing, the mean values of the conversion factors obtained for a portion of nighttime data were thus used to glue the AD and PC data for those parts of the profile where the count rate exceeded 20 MHz. When the mean values of the PC background exceeded 1 MHz (e.g., prior to 2610 UTC in Fig. 2), the AD data (converted to count rate using the conversion factors) were used exclusively without gluing.

b. Water vapor mixing ratio calculation

The water vapor mixing ratio is defined as the mass of water vapor divided by the mass of dry air in a given volume. It is conserved in atmospheric processes that do not involve condensation or evaporation and thus serves as a tracer for air parcels. Also, the vertical profile of mixing ratio strongly influences atmospheric stability. Water vapor mixing ratio can be calculated using the following expression (Whiteman 2003b) by taking the ratio of the Raman water vapor (407.5 nm) and nitrogen signals (386.7 nm) and accounting for the atmospheric differential transmission that occurs at the two different return wavelengths:

$$w = k\,\frac{O_N(r)}{O_H(r)}\,\frac{F_N(T)}{F_H(T)}\,\frac{P(\lambda_H, r)}{P(\lambda_N, r)}\,\frac{\dfrac{d\sigma_N(\pi)}{d\Omega}}{\dfrac{d\sigma_H(\pi)}{d\Omega}}\,\frac{\xi(\lambda_N)}{\xi(\lambda_H)}\,\Delta\tau(\lambda_N, \lambda_H, r), \tag{1}$$

$$k \cong 0.78\frac{\mathrm{MW}_{\mathrm{H_2O}}}{\mathrm{MW}_{\mathrm{DryAir}}} \cong 0.485, \tag{2}$$

where w is the water vapor mixing ratio typically expressed in units of g kg^{-1}, $O_N(r)/O_H(r)$ is the ratio of overlap functions for the N_2 (N) and H_2O (H) channels, k is a proportionality constant determined by the ratio of molecular weights of water ($\mathrm{MW}_{\mathrm{H_2O}}$) and dry air ($\mathrm{MW}_{\mathrm{DryAir}}$) and the fraction of air comprised by molecular nitrogen (~0.78), $F_N(T)/F_H(T)$ is the ratio of the temperature-dependent functions for the Raman N_2 and H_2O channels, where for example $F_H(T)$ is defined by

$$F_H(T) = \frac{\displaystyle\int_{\Delta\lambda_H} \frac{d\sigma_H(\lambda', \pi, T)}{d\Omega}\,\xi(\lambda')\,d\lambda'}{\dfrac{d\sigma_H(\pi)}{d\Omega}\,\xi(\lambda_H)}, \tag{3}$$

and $F_H(T)$ carries all the temperature dependence of the lidar equation for the water vapor channel. It contains the effects of any changes in the system transmission efficiency, $\xi(\lambda)$, for wavelengths other than λ_H within the passband $\Delta\lambda_H$. Here $\xi(\lambda_H)$ is the transmission efficiency at λ_H. The notation $d\sigma_H(\pi)/d\Omega$ is used to indicate the total Raman backscatter cross section for water vapor at the stimulating wavelength. The product $F_H(T)(d\sigma_H(\pi)/d\Omega)$ may be viewed as the effective molecular cross section that is consistent with the use of a monochromatic optical efficiency term, $\xi(\lambda_H)$, in Eq. (1). Here $P(\lambda_X, r) = S(\lambda_X, r) - B(\lambda_X, r)$, where $P(\lambda_X, r)$ is the background-subtracted power in the Raman channel for species X, and S and B represent the signal and background, respectively. Thus, $P(\lambda_H, r)/P(\lambda_N, r)$ is the ratio of background-subtracted signals from the H_2O and N_2 channels, $(d\sigma_N(\pi)/d\Omega)/(d\sigma_H(\pi)/d\Omega)$ is the ratio of the full Raman cross sections for N_2 and H_2O, $\xi(\lambda_N)/\xi(\lambda_H)$ is the ratio of N_2 and H_2O lidar channel efficiencies at their characteristic wavelengths of λ_N and λ_H, and $\Delta\tau(\lambda_H, \lambda_N, r)$ is the differential atmospheric transmission that occurs at the Raman shifted wavelengths λ_N and λ_H. The value of $\Delta\tau$ is determined from

$$\Delta\tau(\lambda_H, \lambda_N, r) = \exp\left\{ -\int_0^r [\alpha(\lambda_H, r') - \alpha(\lambda_N, r')]\,dr' \right\}, \tag{4}$$

where r is the range to the volume of interest, and α is the extinction coefficient (units of inverse length).

The equations used to quantify the random error in the water vapor mixing ratio, assuming Poisson statistics, are given below:

$$\frac{\sigma^2_{R_w}}{R_w^2} = \frac{\sigma^2_{\mathrm{SH}} + \sigma^2_{\mathrm{BH}}}{(S_H - B_H)^2} + \frac{\sigma^2_{\mathrm{SN}} + \sigma^2_{\mathrm{BN}}}{(S_N - B_N)^2}, \tag{5}$$

$$\sigma^2_{R_w} = \frac{(S_H - B_H)^2}{(S_N - B_N)^2}\left[\frac{\sigma^2_{\mathrm{SH}} + \sigma^2_{\mathrm{BH}}}{(S_H - B_H)^2} + \frac{\sigma^2_{\mathrm{SN}} + \sigma^2_{\mathrm{BN}}}{(S_N - B_N)^2}\right]. \tag{6}$$

In these equations, R_w represents the ratio of the background-subtracted water vapor and nitrogen lidar signals. In other words, $R_w = (S_H - B_H)/(S_N - B_N)$, where S_X and B_X are shorthand for $S(\lambda_X, r)$ and $B(\lambda_X, r)$, respectively (Whiteman 2003b).

1) OVERLAP CORRECTION FOR THE WATER VAPOR MIXING RATIO MEASUREMENT

Simple geometrical ray trace considerations indicate that in calculating a quantity from a ratio of two lidar channels that use a common field stop [such as the water vapor and nitrogen signals used in calculating the water vapor mixing ratio given by Eq. (1)], the overlap functions $O_N(r)$ and $O_H(r)$ are equal and thus cancel.

In real applications, however, this ratio does not equal unity in the near field, and a residual overlap function must be determined and applied as a correction to the data. The existence of a residual overlap function appears to be due to the fact that as laser light propagates from the near field to the far field of the telescope, light received by the optical detection system spreads across optical components such as interference filters and photomultiplier tubes that may possess position-dependent efficiencies. These effects are greatest in the near field where modern radiosondes can provide high-quality measurements of relative humidity, temperature, and pressure. For the IHOP analysis, therefore, a mean residual overlap correction function was calculated by using 26 comparisons of SRL and Vaisala RS-80 radiosonde profiles of water vapor mixing ratio that occurred during IHOP. The mean residual overlap correction function resulting from that calculation was then applied to all IHOP water vapor mixing ratio data as a part of the data reduction. The residual overlap correction function was unity above an altitude of 750 m and decreased to 0.94 at an altitude of 300 m, the minimum altitude of processed data for IHOP. Therefore the maximum correction produced by this residual overlap correction function was 6%.

2) Temperature dependence of Raman scattering

The temperature dependence of narrowband water vapor and nitrogen Raman measurements was also accounted for in the analysis of the IHOP water vapor mixing ratio data. An analysis of the temperature dependence of Raman water vapor and nitrogen scattering and its influence on the mixing ratio calculation indicates that 1) the effect is dominated by the temperature dependence of the water vapor spectrum and not the N_2 spectrum and 2) the net effect for likely filter configurations is to yield an apparent excess in water vapor concentrations that tends to increase with altitude (Whiteman 2003a,b). This latter effect is due primarily to a shift of intensity in the Raman spectrum of water vapor toward the band origin as temperatures decrease with altitude.

To assess the magnitude of this effect for the IHOP measurements, laser output and interference filter transmission properties were carefully measured in order to apply the results of the earlier theoretical studies. The Continuum laser frequency-doubled wavelength was measured using a Burleigh 4500 wavemeter and found to be 532.07 $\pm$0.005 nm. Assuming errors are random and uncorrelated, this implies a frequency-tripled wavelength of 354.71 $\pm$ 0.003 nm. In addition, the water vapor and nitrogen interference filter band-

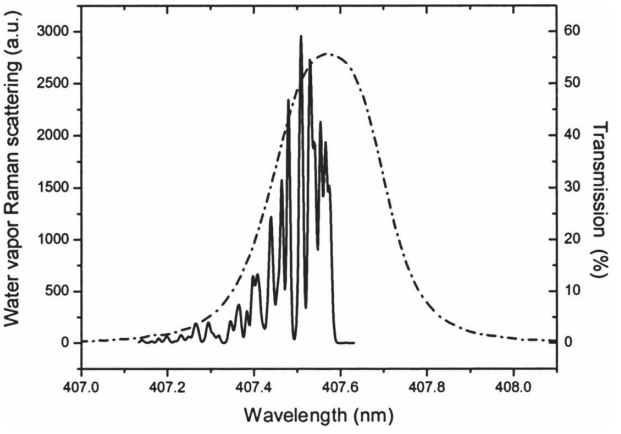

FIG. 3. Water vapor interference filter transmission measurements (shown with a dashed line) using a mercury lamp–calibrated Fourier Transform Spectrometer operating at 0.5 cm^{-1} resolution. For reference, the Raman water vapor spectrum simulated at 270 K is also plotted using a solid line. The shift in the filter from the peak of the Raman spectrum implies significant temperature sensitivity for the water vapor measurement.

pass characteristics were measured using a Thermo-Electron Nicolet 870 Fourier Transform Spectrometer (FTS) operating at 0.5 cm^{-1} resolution. The spectrometer was calibrated using a mercury lamp since the internal calibration based on a Helium Neon (HeNe) laser was found to not be reliable for measurements in the near-UV region of the spectrum (i.e., at shorter wavelengths than the HeNe calibration source). The combined error of the FTS measurement and mercury calibration did not exceed 0.01 nm. Figure 3 shows the mercury lamp calibration corrected measurements of the water vapor interference filter transmission overlaid on the Raman scattering spectrum of water vapor calculated at 270 K using the data from reference (Avila et al. 1999). The figure shows that the peak of the water vapor interference filter used for the IHOP water vapor measurements was shifted long of the peak in the Raman water vapor spectrum by approximately 0.05 nm. (Our comparison of traditional grating spectrometer measurements of filter central position and those obtained with the mercury lamp–calibrated FTS instrument have revealed differences in centerline position of up to 0.05 nm. The FTS measurements are considered more reliable due to the instrument's inherent linear response, the repeatability of the mercury calibration of the FTS, and, in a grating spectrometer, the difficulty of accounting for the sinusoidal variation of spectral position between calibration points.) The fact that the filter was positioned long of the peak of the water vapor spectrum introduced considerable temperature sensitivity to the measurement of water vapor over the range of temperatures present in the tropo-

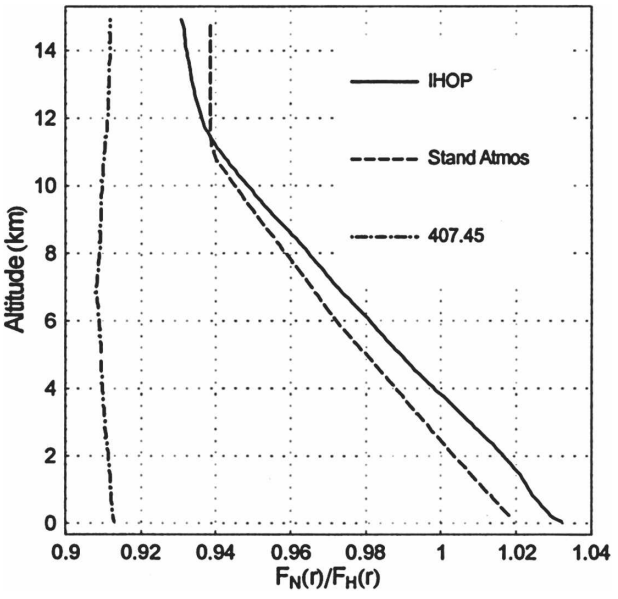

FIG. 4. Temperature correction vectors $F_N\,[T\,(r)]/F_{\rm H}\,[T\,(r)]$ for the water vapor mixing ratio calculation. The vector applied during the IHOP analysis is shown along with the vector corresponding to the *U.S. Standard Atmosphere, 1976* assuming the same experimental configuration as in IHOP. The curve labeled 407.45 is the temperature vector that would result if the water vapor filter had been positioned at 407.45 nm through tilt tuning. This latter configuration is nearly temperature insensitive throughout the troposphere.

sphere as will be shown later. It should be mentioned here that tilting the filter so as to operate at a shorter wavelength such as 407.45 nm would essentially eliminate the temperature dependence of water vapor with altitude. Since the time of the IHOP field campaign, this tilt-tuning has been implemented in the SRL.

A study of the transmission properties of the SRL indicated that all significant variation in the lidar system efficiency over the passband of the Raman water vapor feature was confined to the water vapor interference filter itself. Therefore, the filter transmission measurements versus wavelength can be used to indicate the variation of the lidar system efficiency over the water vapor passband. Similar analysis of the Raman nitrogen measurements were made and combined to generate the mean temperature correction vector, $F_N\,[T\,(r)]/F_H\,[T\,(r)]$ from Eq. (1), that was applied to all the SRL water vapor mixing ratio profiles during the reduction of the IHOP data. This correction vector is shown in Fig. 4. The mean IHOP temperature correction vector varies by approximately 10% from the surface to an altitude of 14 km. This implies that, for the configuration of the SRL during IHOP, the correction to the water vapor mixing ratio due the temperature dependence of Raman scattering is approximately 10% in the troposphere. For comparison, the temperature correction vector calculated for the same filter characteristics but assuming the *U.S. Standard Atmosphere, 1976* temperature profile is also shown. As this comparison implies, the residual error due to using a single temperature correction vector for all of the IHOP data is estimated to be 1% or less. The temperature correction vector for the same set of water vapor and nitrogen filters, but if the water vapor filter had been tilt-tuned to 407.45 nm, is also shown in the figure. Notice that for a filter position of 407.45 nm, the values of the ratio $F_N\,[T\,(r)]/F_H\,[T\,(r)]$ are lower for this nearly temperature insensitive configuration indicating that a larger fraction of the Raman water vapor cross section is being transmitted. Figure 4 demonstrates that for the configuration of IHOP a significant temperature- (and thus altitude-) dependent correction was required for the water vapor mixing ratio calculation. However, the figure also shows that, even for a narrow water vapor interference filter such as used in the SRL for IHOP (0.25 nm), the temperature sensitivity can essentially be eliminated with proper tuning of system parameters if accurate measurements of laser output wavelength and lidar system transmission characteristics are available.

3) WATER VAPOR MIXING RATIO CALIBRATION

A first principles Raman water vapor lidar calibration can be performed with standard optical laboratory procedures. However, the ratio of the Raman cross sections for water vapor and nitrogen is not known to be better than 10%, which implies that the total error of such an effort will exceed 10% (Vaughan et al. 1988; Sherlock et al. 1999). Calibration by comparison with other water vapor sensors, such as research grade radiosonde, microwave radiometer, or GPS, is thus the standard within the Raman water vapor lidar community and the general technique that was used to calibrate the SRL water vapor measurements during IHOP.

In particular, the SRL water vapor mixing ratio measurements during IHOP were calibrated by comparing the integral of the lidar mixing ratio profile with the total precipitable water (PW) derived from a SuomiNet GPS (Ware et al. 2000) system mounted on the SRL. During the daytime, the SRL water vapor profile extended usefully only to the top of the boundary layer, thus leaving a significant fraction of the total precipitable water unmeasured. Therefore to calculate PW from the lidar during the daytime, SRL calibrations with respect to GPS were limited to radiosonde launch times and the radiosonde profile was normalized to the lidar and used to extend the lidar mixing ratio profile

upward beyond the point at which 25% random error was present in the lidar data. To account for the portion of the mixing ratio profile near the ground not measured by the lidar, a linear interpolation was performed between the lowest altitude measured by the lidar (typically 300 m) to the ground point measured by a Paroscientific Met3A station associated with the SuomiNet GPS system. This composite profile was then integrated to yield the SRL total precipitable water for daytime comparisons with GPS. For nighttime comparisons, it was not necessary to extend the profile upward using radiosonde since the lidar water vapor data were of sufficient quality to permit ~99% of the PW to be quantified based on standard atmosphere concentrations of water vapor above the maximum lidar height measured. However, the downward extension to the ground was still necessary.

Except for three dates during IHOP (14, 17, and 18 June), the water vapor data were processed using a single, height-independent calibration constant determined from the GPS calibration procedure just described. On these days, the lidar calibration differed by 10%–15% from the mean calibration value, perhaps due to accidental changes in system operating parameters. For these cases the calibration constant used was the one determined on that day instead of the mean value. The standard deviation of the calibration constant for the IHOP water vapor mixing ratio data, including the effects of these anomalous days, was approximately 6%. When considering only daytime measurements it was approximately 6.5% and 4.5% when considering only nighttime measurements. The smaller standard deviation of the calibration constant for nighttime measurements is thought to be due to greater atmospheric horizontal homogeneity at night and thus the better agreement between the profile of water vapor measured over the lidar site and the volume average measurement of the GPS. The daytime and nighttime calibration constants agreed to within ~1%, implying that there was no significant difference in the lidar water vapor calibration constant due to diurnal effects. It is worth mentioning that there were earlier, preliminary releases of the SRL water vapor data from IHOP that did not include the overlap and temperature correction analysis described here. Researchers who may have used early SRL results from IHOP should retrieve the latest results available from the IHOP archive.

4) GPS AS THE CALIBRATION SOURCE FOR RAMAN WATER VAPOR LIDAR

The U.S. DOE Atmospheric Radiation Measurement (ARM) Program calibrates its Raman lidar, the Climate and Radiation Facility Raman Lidar (CARL), in a similar fashion as just described for the SRL except that the CARL PW is compared to the total column water vapor measured by microwave radiometer (Turner et al. 2002). Research done within the DOE ARM Program indicates that carefully calibrated and analyzed microwave radiometer (MWR) data possess an absolute accuracy of approximately 3%–4%. This makes it an excellent calibration standard for atmospheric research. A deployment of the SRL to the DOE Southern Great Plains site in Oklahoma in 2003 for the Atmospheric Infrared Sounder (AIRS) Water Vapor Experiment-Ground (AWEX-G) (Whiteman et al. 2005) permitted a careful comparison of the ARM microwave radiometer and the same SuomiNet GPS system that accompanied the SRL into the field for IHOP. The GPS measures over a much larger volume than the MWR and therefore individual comparisons can show considerable disagreement under conditions of spatial nonhomogeneity in the atmosphere. Line-of-sight comparisons of the two instruments have been performed to address these differences and have shown excellent agreement (Braun et al. 2003). During AWEX-G, we performed an extended comparison of 30-min average GPS and MWR vertical precipitable water measurements in order to minimize the effects of short-term spatial inhomogeneities. The results of that comparison (Whiteman et al. 2005) showed that in the mean the GPS PW was 2.4% higher than the MWR PW and that there was no significant diurnal bias between the two sensors. This overall agreement of the two sensors is within the uncertainty of the MWR, supporting the use of the GPS system as an independent source for calibration of Raman water vapor lidar measurements.

c. *Aerosol scattering ratio and backscatter coefficient*

The aerosol scattering ratio, R, is defined as the ratio of the total (molecular and particle) backscatter coefficient divided by the molecular backscatter coefficient. It can be calculated from the ratio of the received power in the Rayleigh–Mie and Raman vibrational N_2 channels. The equations for calculating the aerosol scattering ratio, including the effects of the temperature dependence of rotational and vibrational scattering, are (Whiteman 2003b)

$$\mathcal{R}(\lambda_L, r) - 1 = C_N^*(\lambda_L, r) F_N[T(r)] \frac{P(\Delta\lambda_R, r)}{P(\Delta\lambda_N, r)} \Delta\tau(\lambda_N, \lambda_L, r) - F_R[T(r)], \quad (7)$$

$$C_N^*(\lambda_L, r) = C_N(\lambda_L) \frac{O_N(r)\xi(\lambda_N)}{O_R(r)\xi(\lambda_L)}, \quad (8)$$

$$C_N(\lambda_L = 355) \simeq 0.78 \frac{d\sigma_N(\pi)/d\Omega(\lambda_L = 355)}{d\sigma_{\text{mol}}(\pi)/d\Omega(\lambda_L = 355)}$$

$$\simeq 0.78 \frac{2.8 \times 10^{-30}}{3.2 \times 10^{-27}} \simeq 6.8 \times 10^{-4}, \quad (9)$$

where $P\ (\Delta\lambda_R, r)$ and $P\ (\Delta\lambda_N, r)$ are the background-subtracted received power in the channels measuring the Rayleigh–Mie signal in the spectral band $\Delta\lambda_R$ and the vibrational N_2 Raman-shifted in the spectral band $\Delta\lambda_N$. The differential transmission, $\Delta\tau\ (\lambda_N, \lambda_L, r)$, is the ratio of atmospheric transmission at the two wavelengths, λ_N and λ_L, and is calculated using an equation similar to (4). The lidar channel optical efficiencies are expressed as $\xi\ (\lambda_N)$ and $\xi\ (\lambda_L)$. The lidar system overlap functions are given by $O_N\ (r)$ and $O_R\ (r)$. The calibration constant C_N has been evaluated at the laser wavelength of ~355 nm using the values of the Raman vibrational and Rayleigh differential scattering cross sections, $d\sigma_N(\pi)/d\Omega$ and $d\sigma_{\text{mol}}(\pi)/d\Omega$, respectively (Measures 1984). The effect of the temperature dependence of the Raman scattering on the Rayleigh–Mie and Raman nitrogen signals is contained in the two terms, $F_R\ [T\ (r)]$ and $F_N\ [T\ (r)]$, respectively, which are calculated using an equation similar to (3). The aerosol backscatter coefficient, $\beta^{\text{aer}}(\lambda_L, r)$, can be evaluated from the aerosol scattering ratio as follows:

$$\beta^{\text{aer}}(\lambda_L, r) = \beta_\pi^{\text{mol}}(\lambda_L, r)(\mathcal{R}(\lambda_L, r) - 1), \quad (10)$$

where $\beta_\pi^{\text{mol}}(\lambda_L, z)$ is the Rayleigh backscatter coefficient at the laser wavelength calculated using density measurements from a radiosonde.

d. Cirrus cloud optical depth and layer mean extinction to backscatter ratio

Cirrus cloud optical depth can be calculated from a Raman lidar measurement of molecular nitrogen, which, if properly performed, shows only attenuation due to the presence of the cloud. The amount of this attenuation can be converted to optical depth once the atmospheric density is known. The single scattering equation that yields two-way optical depth is obtained by integrating the equation for aerosol extinction (Whiteman 2003a) and can be written as

$$\int_{r_1}^{r_2} [\alpha(\lambda_L, r) + \alpha(\lambda_N, r)]\ dr \quad (11)$$

$$= \ln\left[\frac{O_N(r_2)F_N(T(r_2))N_N(r_2)}{O_N(r_1)F_N(T(r_1))N_N(r_1)} \frac{r_1^2 P(\lambda_N, r_1)}{r_2^2 P(\lambda_N, r_2)}\right]$$

$$- \int_{r_1}^{r^2} [\alpha_{\text{mol}}(\lambda_L, r) + \alpha_{\text{mol}}(\lambda_N, r)]\, dr \quad (12)$$

$$\approx \ln\left[\frac{N_N(r_2)\, r_1^2 P(\lambda_N, r_1)}{N_N(r_1)\, r_2^2 P(\lambda_N, r_2)}\right] - \int_{r_1}^{r_2} [\alpha_{\text{mol}}(\lambda_L, r) + \alpha_{\text{mol}}(\lambda_N, r)]\, dr, \quad (13)$$

where r_1 is an altitude level below the cloud, r_2 is above the cloud, λ_L is the laser wavelength (354.7 nm), λ_N is the wavelength of the Raman nitrogen signal (386.7 nm), $\alpha(\lambda_x, r)$ is the cloud extinction coefficient as a function of wavelength and range, $O_N\ (r)$ is the overlap function for the nitrogen channel evaluated at range r, $F_N\ [T\ (r)]$ is the temperature-dependent factor for the Raman nitrogen measurement, $N_N\ (r)$ is the number density of atmospheric nitrogen (using the full atmospheric number density yields equivalent results) as a function of range, $P\ (\lambda_N, r)$ is the background-subtracted Raman lidar nitrogen signal, and $\alpha_{\text{mol}}(\lambda_x, r)$ is the extinction coefficient due to molecular scattering obtained from radiosonde data. At typical cirrus altitudes, the ratios of the overlap and temperature-dependent factors are nearly unity and can be ignored as shown in the final form of Eq. (13), which is the same result that would be obtained by integrating the traditional aerosol extinction equation (Ansmann et al. 1992). Assuming no multiple scattering and that cirrus cloud extinction is wavelength insensitive between λ_L and λ_N, the optical depth of the cloud is simply one-half of Eq. (13).

A modified approach to the evaluation of Eq. (13) was used here and implements an iterative procedure that corrects for the influence of multiple scattering (Whiteman et al. 2001a) using a Gaussian approximation technique (Eloranta 1998) and calculates a layer mean particle radius in the process. The integrated backscatter is determined by integrating the profile of cirrus cloud backscatter coefficient, which has been shown to be essentially insensitive to multiple scattering (Wandinger 1998). The layer mean extinction to backscatter ratio, also known as the lidar ratio, is then just the ratio of the cloud optical depth and the integrated backscatter coefficient.

e. Aerosol depolarization

The ability to calculate scattering ratios using the Raman lidar technique permits both the volume and particle depolarization ratios δ_{vol} and δ_{par} to be calculated (Behrendt and Nakamura 2002) as follows:

$$\delta_{\text{vol}}(z) = \frac{\beta_\perp^{\text{mol}}(z) + \beta_\perp^{\text{par}}(z)}{\beta_\parallel^{\text{mol}}(z) + \beta_\parallel^{\text{par}}(z)} = \frac{R_\perp(z)}{R_\parallel(z)}\, \delta_{\text{mol}}(z), \quad (14)$$

$$\delta_{\text{par}}(z) = \frac{\beta_\perp^{\text{par}}(z)}{\beta_\parallel^{\text{par}}(z)} = \frac{R_\perp(z) - 1}{R_\parallel(z) - 1}\, \delta_{\text{mol}}(z), \quad (15)$$

where β refers to the backscatter coefficients for either molecules (mol) or particles (par) in either the perpendicular ($\perp$) or parallel ($\parallel$) directions; $R_\perp$ is the scattering ratio for the perpendicular polarization signal; and $R_\parallel$ is the scattering ratio for the parallel polarized signal. The equation for the scattering ratio used here is given in (7) and fully accounts for both the temperature dependence of Raman scattering as described in section 4c.

The aerosol depolarization measurements were calibrated by first determining the relative gain of the parallel and perpendicular channels by observing a fully depolarized source, in this case thick overcast skies. Using this value of the relative gain in the channels, the volume depolarization ratio in clear air was found to be ~1.7% as opposed to the theoretical value of molecular depolarization of ~0.5% that corresponds to our ~0.05 nm bandpass filters. The additional depolarization was attributed to misalignment between the planes of polarization of the outgoing laser and the polarization analyzer (Reichardt et al. 2003). To compensate for the resulting cross talk between the parallel and perpendicular channels, an approximate correction technique was used here. The volume depolarization ratio was calculated assuming variable amounts of cross talk between the parallel and perpendicular channels using the following approximate technique.

Let the measured signals in the parallel and perpendicular channels in the presence of cross talk due to small angular mistuning of the receiver system be expressed as $I_\parallel$ and $I_\perp$ as follows:

$$I_\perp = G[\cos^2(\theta)\beta_\perp^{\mathrm{mol}} + \sin^2(\theta)\beta_\parallel^{\mathrm{mol}}], \quad (16)$$

$$I_\parallel = [\cos^2(\theta)\beta_\parallel^{\mathrm{mol}} + \sin^2(\theta)\beta_\perp^{\mathrm{mol}}], \quad (17)$$

where G is the relative gain of the two channels and θ is the difference in angle of the receiver coordinates and the transmitter coordinates due to mistuning of the polarization beamsplitter. In clear air the volume depolarization ratio is then given by

$$\delta_{\mathrm{vol}}(z) = \frac{I_\perp}{I_\parallel} = \frac{G[\cos^2(\theta)\beta_\perp^{\mathrm{mol}} + \sin^2(\theta)\beta_\parallel^{\mathrm{mol}}]}{\cos^2(\theta)\beta_\parallel^{\mathrm{mol}} + \sin^2(\theta)\beta_\perp^{\mathrm{mol}}}. \quad (18)$$

This expression makes the approximation that all depolarization is due to angular misalignment of the receiver optics and that no other sources contribute. Solving this equation for θ given the actual measured minimum depolarization of ~1.7% yielded an angular difference of ~3° between the laser polarization and the position of the polarization analyzer. This amount of assumed cross talk was assumed in the analysis of the depolarization data presented in Part II. Another correction that was applied to the depolarization data was to account for the variation in the molecular depolarization as a function of temperature (Behrendt and Nakamura 2002). The value of molecular depolarization for the filters in use and the range of temperatures observed during IHOP was found to vary as a function of temperature from approximately 0.46% to 0.52%.

5. Summary

NASA GSFC participated in the first International H_2O Project in May–June 2002. A new configuration of the SRL enabled measurements of water vapor, aerosol backscatter, extinction, depolarization, liquid water, ice water, and rotational Raman temperature. In particular the combination of narrow field of view, narrow spectral bandpass, relatively large pulse energy Nd:YAG laser, and both analog and photon-counting detection electronics permitted a single configuration to be used for both daytime and nighttime measurements of water vapor mixing ratio. The improved water vapor measurement capability permits convective boundary layer processes to be studied throughout the diurnal cycle. In this first of two parts, the method of joining the analog and photon-counting data, referred to as "gluing," was described for the case of water vapor measurements during a period that included a large number of atmospheric waves. For the first time, the temperature dependence of Raman scattering was accounted for in the calibration of a Raman water vapor and aerosol lidar and shown, for the configuration of the SRL during IHOP, to affect the upper-tropospheric water vapor measurements by approximately 10%. A study of the calibration of water vapor mixing ratio indicated a stable calibration constant to within 1% between daytime and nighttime measurements. The measurements presented here were all provided using a single output wavelength of 354.7 nm demonstrating the feasibility of offering all of these measurements in an automated, eye-safe Raman lidar system. In Part II, comparisons of SRL measurements with other sensors are presented along with daytime and nighttime case studies.

Acknowledgments. The authors thank the NASA Interdisciplinary Program managed by Dr. Jim Dodge for its support of this activity.

REFERENCES

Ansmann, A., M. Riebesell, U. Wandinger, C. Weitkamp, E. Voss, W. Lhamann, and W. Michaelis, 1992: Combined Raman elastic-backscatter LIDAR for vertical profiling of moisture, aerosol extinction, backscatter and LIDAR ratio. *Appl. Phys.,* **B55,** 18–28.

Avila, G., J. M. Fernandez, B. Mate, G. Tejeda, and S. Montero,

1999: Rovibrational Raman cross sections of water vapor in the OH stretching region. *J. Mol. Spectr.,* **196,** 77–92.

Behrendt, A., and T. Nakamura, 2002: Calculation of the calibration constant of polarization lidar and its dependency on atmospheric temperature. *Opt. Express,* **10,** 805–817.

Bisson, S. E., J. E. M. Goldsmith, and M. G. Mitchell, 1999: Narrow-band, narrow-field-of-view Raman lidar with combined day and night capability for tropospheric water-vapor profile measurements. *Appl. Opt.,* **38,** 1841–1849.

Braun, J., C. Rocken, and J. Liljegren, 2003: Comparisons of line-of sight water vapor observations using the global positioning system and a pointing microwave radiometer. *J. Atmos. Oceanic Technol.,* **20,** 606–612.

Cooney, J., K. Petri, and A. Salik, 1985: Measurements of high-resolution atmospheric water-vapor profiles by use of a solar blind Raman lidar. *Appl. Opt.,* **24,** 104–108.

Di Girolamo, P., R. Marchese, D. N. Whiteman, and B. B. Demoz, 2004: Rotational Raman lidar measurements of atmospheric temperature in the UV. *Geophys. Res. Lett.,* **31,** L01106, doi:10.1029/2003GL018342.

Ellingson, R. G., and W. J. Wiscombe, 1996: The spectral radiance experiment (SPECTRE): Project description and sample results. *Bull. Amer. Meteor. Soc.,* **77,** 1967–1985.

Eloranta, E. W., 1998: Practical model for the calculation of multiply scattered lidar returns. *Appl. Opt.,* **37,** 2464–2472.

Feltz, W. F., W. L. Smith, R. O. Knuteson, H. E. Revercomb, H. M. Woolf, and H. B. Howell, 1998: Meteorological applications of temperature and water vapor retrievals from the ground-based Atmospheric Emitted Radiance Interferometer (AERI). *J. Appl. Meteor.,* **37,** 857–875.

Ferrare, R., and Coauthors, 2000: Comparison of aerosol optical properties and water vapor among ground and airborne lidars and sunphotometers during TARFOX. *J. Geophys. Res.,* **105** (D8), 9917–9933.

Gentry, B. M., H. Chen, S. Li, S. Mathur, J. Dobler, W. Hasselbrack, and J. Comer, 2004: Wind profiles obtained with a molecular direct detection Doppler LIDAR during IHOP_2002. *Proc. 22d Int. Laser Radar Conf. (ILRC2004),* Matera, Italy, European Space Agency, ESA SP-561, 731–733.

Goldsmith, J. E. M., and R. A. Ferrare, 1994: Performance modeling of daytime Raman lidar systems for profiling atmospheric water vapor. *Proc. 16th Int. Laser Radar Conf.,* Part 2, NASA Conf. Publication 3158, 667–670.

Holben, B. N., and Coauthors, 1998: AERONET—A federated instrument network and data archive for aerosol characterization. *Remote Sens. Environ.,* **66,** 1–16.

Measures, R. M., 1984: *Laser Remote Sensing Fundamentals and Applications.* Wiley-Interscience, 510 pp.

Reichardt, J., R. Baumgart, and T. J. McGee, 2003: Three-signal method for accurate measurements of depolarization ratio with lidar. *Appl. Opt.,* **42,** 4909–4913.

Renaut, D., and R. Capitini, 1988: Boundary layer water vapor probing with a solar-blind Raman lidar: Validations, meteorological observations and prospects. *J. Atmos. Oceanic Technol.,* **5,** 585–601.

——, J. C. Pourny, and R. Capitini, 1980: Daytime Raman-lidar measurements of water-vapor. *Opt. Lett.,* **5,** 233–235.

Russo, F., D. N. Whiteman, B. Demoz, Z. Wang, I. Veselovskii, and R. Hoff, 2004: Development of Raman lidar techniques to address the aerosol indirect effect: The liquid water content of clouds. *Proc. 22d Int. Laser Radar Conf.,* Matera, Italy, European Space Agency, Vol. I, ESA SP-561.

Schwemmer, G., D. O. Miller, T. D. Wilkerson, and S. Lee, 2004: Lidar data products enabled by conical scanning: HARLIE measurements during IHOP. *Proc. 22d Int. Laser Radar Conf.,* Matera, Italy, European Space Agency, Vol. I, ESA SP-561, 17–20.

Sherlock, V., A. Hauchecorne, and J. Lenoble, 1999: Methodology for the independent calibration of Raman backscatter water-vapor lidar systems. *Appl. Opt.,* **38,** 5816–5837.

Turner, D. D., R. A. Ferrare, L. A. H. Brasseur, and W. F. Feltz, 2002: Automated retrievals of water vapor and aerosol profiles from an operational Raman lidar. *J. Atmos. Oceanic Technol.,* **19,** 37–50.

Vaughan, G., D. P. Wareing, L. Thomas, and V. Mitev, 1988: Humidity measurements in the free troposphere using Raman backscatter. *Quart. J. Roy. Meteor. Soc.,* **114,** 1471–1484.

Wandinger, U., 1998: Experimental determination of the lidar overlap profile with Raman lidar. *Appl. Opt.,* **37,** 417–427.

Wang, J., D. J. Carlson, D. B. Parsons, T. F. Hock, D. Lauritsen, H. L. Cole, K. Beierle, and E. Chamberlain, 2003: Performance of operational radiosonde humidity sensors in direct comparison with a chilled mirror dew-point hygrometer and its climate implication. *Geophys. Res. Lett.,* **30,** 1860, doi:10.1029/2003GL016985.

Wang, Z., D. N. Whiteman, B. B. Demoz, and I. Veselovskii, 2004: A new way to measure cirrus cloud ice water content by using ice Raman scatter with Raman lidar. *Geophys. Res. Lett.,* **31,** L15101, doi:10.1029/2004GL020004.

Ware, R. H., and Coauthors, 2000: SuomiNet: A real-time national GPS network for atmospheric research and education. *Bull. Amer. Meteor. Soc.,* **81,** 677–694.

Weckwerth T. M., and Coauthors, 2004: An overview of the International H2O Project (IHOP_2002) and some preliminary highlights. *Bull. Amer. Meteor. Soc.,* **85,** 253–277.

Whiteman, D. N., 2003a: Examination of the traditional Raman lidar technique. I. Evaluating the temperature-dependent lidar equations. *Appl. Opt.,* **42,** 2571–2592.

——, 2003b: Examination of the traditional Raman lidar technique. II. Evaluating the ratios for water vapor and aerosols. *Appl. Opt.,* **42,** 2593–2608.

——, and S. H. Melfi, 1999: Cloud liquid water, mean droplet radius and number density measurements using a Raman lidar. *J. Geophys. Res.,* **104,** 31 411–31 419.

——, ——, and R. A. Ferrare, 1992: Raman lidar system for the measurement of water vapor and aerosols in the earth's atmosphere. *Appl. Opt.,* **31,** 3068–3082.

——, and Coauthors, 2001a: Raman lidar measurements of water vapor and cirrus clouds during the passage of Hurricane Bonnie. *J. Geophys. Res.,* **106,** 5211–5225.

——, G. Schwemmer, T. Berkoff, H. Plotkin, L. Ramos-Izquierdo, and G. Pappalardo, 2001b: Performance modeling of an airborne Raman water vapor lidar. *Appl. Opt.,* **40,** 375–390.

——, S. H. Melfi, R. A. Ferrare, and K. D. Evans, 1994: Daytime measurements of water vapor mixing ratio using Raman scattering—Techniques and assessment. *Extended Abstracts, 17th Int. Laser Radar Conf.,* Sendai, Japan, 137–140.

——, and Coauthors, 2005: The AIRS Water Vapor Experiment (AWEX-G) and its relationship to aqua validation. *J. Geophys. Res*., in press.

——, and Coauthors, 2006: Raman water vapor lidar measurements during the International H_2O Project. Part II: Instrument comparisons and case studies. *J. Atmos. Oceanic Technol.,* **23,** 170–183.